Journal of Materials Chemistry A

ROYAL SOCIETY OF CHEMISTRY

PAPER

View Article Online
View Journal | View Issue

Cite this: J. Mater. Chem. A, 2023, 11, 12958

Stabilizing Ni-rich high energy cathodes for advanced lithium-ion batteries: the case of $LiNi_{0.9}Co_{0.1}O_2$†

Francis Amalraj Susai,‡[a] Amreen Bano,‡[a] Sandipan Maiti,[a] Judith Grinblat,[a] Arup Chakraborty,[a] Hadar Sclar,[a] Tatyana Kravchuk,[b] Aleksandr Kondrakov,[c] Maria Tkachev,[a] Michael Talianker,[d] Dan Thomas Major,*[a] Boris Markovsky*[a] and Doron Aurbach*[a]

Lithiated oxides like $Li[Ni_xCo_yMn_z]O_2$ ($x + y + z = 1$) with high nickel content ($x \geq 0.8$) can possess high specific capacity ≥200 mA h g^{-1} and have attracted extensive attention as perspective cathode materials for advanced lithium-ion batteries. In this work, we synthesized $LiNi_{0.9}Co_{0.1}O_2$ (NC90) materials and studied their structural characteristics, electrochemical performance, and thermal behavior in Li-cells. We developed modified cationic-doped NC90 samples with greatly improved properties due to doping with Mo^{6+} and B^{3+} and dual doping *via* simultaneous modification with these dopants. The main results of the current study are significantly higher capacity retention, greatly reduced voltage hysteresis, and considerably decreased charge-transfer resistance of the Mo and Mo–B doped electrodes compared to the undoped ones upon prolonged cycling. We also revealed remarkable microstructural stability of the Mo-doped electrodes, whereas the undoped samples were unstable and exhibited networks of cracks developed upon cycling. Using density functional theory, we modeled the electronic structure of the undoped, Mo, B single-doped, and Mo–B dual-doped samples and established that the Ni-site is preferred over Co and Li sites. Additionally, density functional theory-based bonding strength calculations suggest that the dopants form strong bonds with oxygen, possibly reducing oxygen release from the cathode. An important finding is that B-dopant tends to segregate to the surface of NC90 similarly to that in NCM85 materials, as shown in our previous reports. In conclusion, this study presents a general approach for effectively stabilizing high-energy Ni-rich layered cathodes charged up to 4.3 V.

Received 25th January 2023
Accepted 21st March 2023

DOI: 10.1039/d3ta00444a

rsc.li/materials-a

10th anniversary statement

On behalf of our colleagues from the Electrochemistry Group, Institute of Nanotechnology and Advanced Materials of Bar-Ilan University, BIU center for Energy and Sustainability and INERC – Israel National Energy Research Consortium, the authors of this paper would like to congratulate the *J. Mater. Chem. A*, its editors and board members on the 10th anniversary of this important journal. Over this decade, the journal contributed so much to the broad field of materials science and to the materials research community. We praise the effective and honest reviewing processes and the high quality of the papers being published therein. We were proud to publish many papers in this prestigious journal, we were also honored to review many high-quality reports in materials science, energy related fields and beyond for this journal. We express here our gratitude to the excellent team that handle the journal, reviewing and publication processes. We are very happy to submit this paper to this *Themed Issue* and believe it can interest a wide spectrum of the interdisciplinary communities involved in materials science, new materials for energy storage, computational modeling, and electrochemistry.

1. Introduction

One of the main challenges in the field of advanced lithium-ion batteries (LIBs), especially for electric vehicles (EVs), is the development of new materials for the positive electrodes (cathodes).[1–5] Cathode materials of layered, spinel and olivine-type structures can deliver high cycling performance and meet current requirements for LIBs for EVs.[3,5–13] An important class of layered structure materials are lithiated oxides consisting of the transition metals Ni, Co, and Mn and having the general

[a]Department of Chemistry, Institute for Nanotechnology and Advanced Materials (BINA), Bar-Ilan University, Ramat-Gan 52900, Israel. E-mail: Doron.Aurbach@biu.ac.il; markovskyboris22@gmail.com; majort@biu.ac.il

[b]Solid State Institute, Technion – Israel Institute of Technology, Haifa 32000, Israel

[c]BASF SE, Carl-Bosch-Str. 38, 67056 Ludwigshafen, Germany

[d]Department of Materials Engineering, Ben-Gurion University of the Negev, Beer-Sheva 84105, Israel

† Electronic supplementary information (ESI) available. See DOI: https://doi.org/10.1039/d3ta00444a

‡ These authors contributed equally.

formulae $Li[Ni_xCo_yMn_z]O_2$ ($x + y + z = 1$, NCM, $R\bar{3}m$ space group). Ni-rich NCM materials (nickel content ≥80 at%) have attracted much attention from R&D groups globally due to specific capacities of ≥200 mA h g^{-1}. This high capacity results from nickel serving as the main electroactive species in the host structure of NCM, undergoing two-electron redox reactions ($Ni^{2+} \leftrightarrow Ni^{3+} \leftrightarrow Ni^{4+}$).[14–16] It has been shown by Manthiram *et al.*[3,12] that cathodes based on these Ni-rich NCM materials or Li and Mn-rich layered oxides enable longer driving-range EVs. However, despite the promise of Ni-rich NCM materials, recent scientific reports demonstrated a vital need to improve several intrinsic drawbacks of these NCM materials: low electronic and ionic conductivities, structural instability, fast capacity decay, high voltage hysteresis, and insufficient rate capability.[17–21] It is well accepted in the literature that material modification approaches are surface coatings with metal oxides or salts (for instance, Al_2O_3, ZrO_2, $AlPO_4$, Li_3PO_4, $Li_2AlZr(PO_4)_3$) and lattice doping of NCMs with mono- and multi-valence cations (for example, Ag^+, Mg^{2+}, Cu^{2+}, Al^{3+}, Ga^{3+}, Cr^{3+}, B^{3+}, Fe^{3+}, Ti^{4+}, Sn^{4+}, Zr^{4+}, Ta^{5+}, Nb^{5+}, W^{6+}, and Mo^{6+}). They result in improved structural and interfacial stability of Ni-rich materials and can resolve shortcomings.[16,22–29] Doping with anions like F^-, Cl^-, and S^{2-} has also facilitated stable cycling performance of Ni-rich cathodes.[23,30,31]

In the current work, we aimed to study high-Ni and low-Co content lithiated oxides $LiNi_{0.9}Co_{0.1}O_2$ (90 and 10 at%, respectively, NC90) in terms of their electrochemical performance in half-cells (*vs.* Li-anodes) and full cells (*vs.* graphite anodes). Cobalt plays an important role in $Li[Ni_xCo_yMn_z]O_2$ materials. It enhances ionic and electronic conductivities and hence rate capability and improves structural characteristics, low-temperature behavior, and thermal stability.[32] The total removal of cobalt from NCM materials results in the deterioration of their positive characteristics and limits, thus the commercial application of Co-free cathodes.[32] Several compositions of NCMs with nickel content close to 90 at% that include small amounts of both Co and Mn and dopants (Mg, Al) has been proposed by Manthiram and co-workers (for instance, $LiNi_{0.890}Mn_{0.055}Co_{0.055}O_2$ (NCM-89), $LiNi_{0.883}Co_{0.053}Al_{0.064}O_2$ (NCA-89), $LiNi_{0.890}Mn0_{.044}Co_{0.042}Al_{0.013}Mg_{0.011}O_2$ (NMCAM-89), and $LiNi_{0.883}Mn_{0.056}Al_{0.061}O_2$ (NMA-89)).[33] It was pointed out that Co played some advantageous roles in NCMs, such as good electronic conduction and reduced Li/Ni mixing for facile ionic conduction. However, as it follows from the literature, Co^{3+} does not seem beneficial in improving electrochemical, structural, and thermal stability in $LiNiO_2$ (LNO) by doping up to 10%.[34] The above issues regarding cobalt's exact role and requirement in low-cobalt or cobalt-free high-nickel layered cathodes are currently under discussion in LIBs.[35]

The present work, which continues our methodical research on synthesis and studies of electrochemical performance, electronic properties, surface segregation phenomena, post-cycling analysis, and theoretical modeling of high-Ni NCMs, is focused on NC90 samples, containing only 10% of Co and doped with Mo^{6+} and B^{3+}. These dopants were chosen because of their significant positive effects on Ni-rich NCMs, as reported by several authors. For instance, Konishi *et al.*[36] demonstrated that partial substitution of manganese by Mo^{6+} in NCM811 suppressed the structural transformation from layered-to-spinel-to-rock-salt phases and improved the thermal stability of the doped samples in reactions with electrolyte solutions. Recently, H. Zhu *et al.*[37] reported on optimal Mo-doped $LiNi_{0.89}Co_{0.1}Mo_{0.01}O_2$ cathode materials with high discharge capacity and enhanced cycling behavior even at a 5C rate. Furthermore, a boron-doping strategy was proposed by Sun *et al.* in 2018, revealing that the B^{3+} dopant can modify the surface energy of high-Ni materials, releasing thus some of the intrinsic internal strain associated with the H2 to H3 hexagonal phase transition at the end of charge to 4.3 V.[18] Additionally, these authors suggested a new class of Mn-free, binary boron-doped materials $Li[Ni_{0.9}Co_{0.1}]O_2$ for advanced LIBs.[38] Feng *et al.* reported on "a three-in-one strategy" of modification of NCM811 material (80% Ni, 10% Co, and 10% Mn) by dual doping with zirconium and boron (using ZrB_2 as dopant precursor) and forming an interfacial coating comprising Li–Zr species. The modified cathodes exhibited superior cycling behavior and improved thermal stability.[39] Dual doping has been considered a more effective means to improve the structural stability of nickel-rich layered materials and enhance the electrochemical behavior of the corresponding electrodes in Li-cells. There are a few reports on high-nickel NCM cathodes dually doped with cations like lanthanum and aluminum,[40] zirconium and aluminum,[41,42] and zirconium and gallium.[43] A couple of Zr^{4+} and Al^{3+} dopants effectively decreased the cationic mixing, anisotropic lattice changes, and microstructural cracking in $LiNi_{0.83}Co_{0.12}Mn_{0.05}O_2$ particles upon charge–discharge cycling of these high-Ni electrodes.[42]

Recently, we have also synthesized and studied a family of several Ni-rich materials NCM811, in which Ni or both Ni and Mn were partially substituted with minor amounts (1–3 mol%) of the molybdenum Mo^{6+}-dopant and NCM85 (85% Ni, 10% Co, and 5% Mn) doped with B^{3+}.[44] These works revealed the positive effect of Mo^{6+} allowing stable cycling behavior of NCM811 and NCM85 cathodes, lowering their voltage hysteresis, charge-transfer (interfacial) impedance, and heat evolution in reactions with battery solutions.[45,46] One of the main findings in our recent work on NCM85 materials doped with B^{3+} was that B-doping enhanced the electrochemical performance, lowered the self-discharge of the above cathodes, and prevented significant microstructural changes cracking across grains upon cycling in the doped samples compared to the undoped ones.[44] To our knowledge, no reports discuss the synthesis, structural characteristics, electrochemical performance, and thermal properties of Ni-rich NCM cathode materials (Ni ≥ 0.8) dually doped with Mo^{6+} and B^{3+} cations. Therefore, based on our promising results obtained with Mo^{6+} and B^{3+} doped Ni-rich cathodes, we were motivated to synthesize and study $LiNi_{0.9}Co_{0.1}O_2$ materials with high-Ni (90%) and low-Co (10%) content. The main goal was to elucidate the impact of high-valence state molybdenum Mo^{6+} and low-valence state boron B^{3+} dopants, as well as dual doping with these cations on structural and electronic characteristics, metal–oxygen bonding, dopants segregation to the surface in the above oxides, electrochemical behavior, and thermal reactions of NC90 cathodes in the

charged state (4.3 V) with battery solutions. The present work contains new findings on NC90 high-Ni cathodes modified by single and dual doping with Mo^{6+} and B^{3+} cations. Despite the extensive work in the field and the reports in the literature about so many types of cathode materials for Li ion batteries, we provide herein a comprehensive information on new materials and describe a very systematic work. The results we obtained from several channels of information – electrochemical, structural, thermal, impedance measurements are very coherent and conclusive. These results – both experimental and computational models – will advance the knowledge and future development of complex electrode systems for advanced, high energy density rechargeable lithium batteries.

2. Results and discussion

2.1 Chemical composition, structural and morphological characteristics of $LiNi_{0.9}Co_{0.1}O_2$ materials

The results of the chemical analysis of the synthesized NC90 materials demonstrate that the compositions of the synthesized samples are close to the desired ones (Table S1†). Their chemical formulae can be represented as follows: $LiNi_{0.9}Co_{0.1}O_2$, $Li[(Ni_{0.9}Co_{0.1})_{99.5}Mo_{0.5}]O_2$, $Li[(Ni_{0.9}Co_{0.1})_{99.5}B_{0.5}]O_2$ and $Li[(Ni_{0.9}Co_{0.1})_{99.5}Mo_{0.25}B_{0.25}]O_2$.

The synthesized compounds' morphological microscopic images obtained by HRSEM are presented in Fig. 1a–d. Typically, the compounds are ball-shaped micron-sized

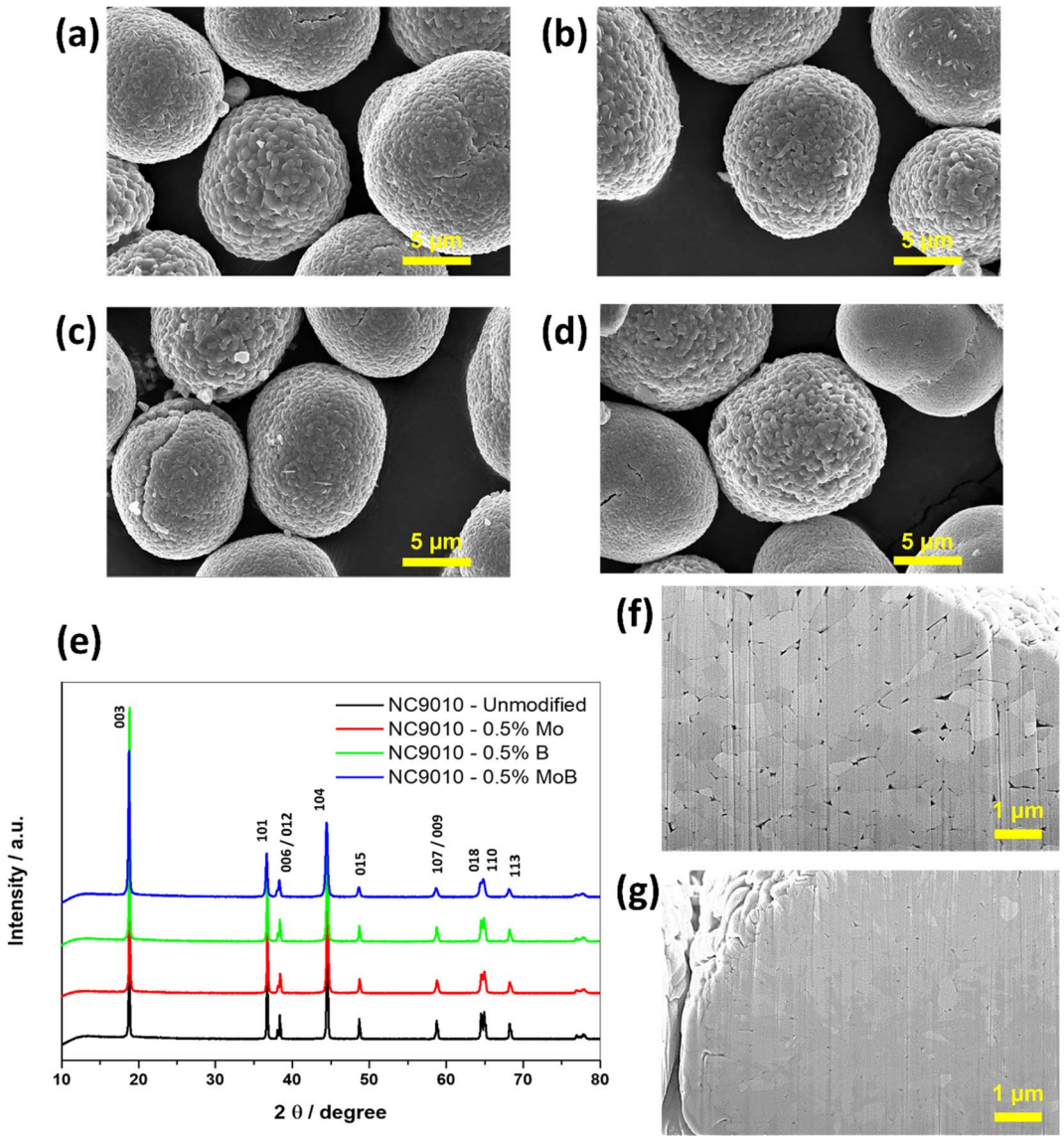

Fig. 1 Morphological microscopic images obtained by HRSEM of the synthesized NC90 materials: (a) undoped, (b)–(d) doped, respectively, with Mo (0.5 mol%), B (0.5 mol%), and dual doped with Mo–B (0.25 mol% of each dopant). The machine setting parameters for HRSEM studies were as follows: det TLD; HV 15.00 kV; WD 5.0 nm; curr 0.4 nA; mag 10 000×; mode SE; HFW 29.8 micron; tilt 0 deg; Magellan BINA. (e) XRD profiles of NC90 material undoped, doped with 0.5 mol% Mo, doped with 0.5 mol% B and dual-doped with 0.25 mol% Mo and 0.25 mol% B. (f) Cross-sectional SEM images of NC90 undoped and (g) 0.5 mol% Mo-doped pristine materials.

Table 1 The unit cell parameters of undoped NC90 and single Mo, B, and dual Mo–B doped materials and the corresponding ratios of the integrated intensities of 003, 104, and (012 + 006)/101 reflections were calculated using the Rietveld refinement. Cell parameters and volume values were determined with a standard deviation of about 0.0001 and 0.001, respectively

Materials	Cell parameters (Å)	Cell volume $(Å)^3$	Ratio I_{003}/I_{104}	Ratio $(I_{012} + I_{006})/I_{101}$	Reliability factor R_p (%)
NC90 undoped	$a = 2.8731$ $c = 14.1863$	101.41	1.22	0.41	1.70
NC90 0.5 mol% Mo-doped	$a = 2.8732$ $c = 14.1860$	101.42	1.35	0.40	1.84
NC90 0.5 mol% B-doped	$a = 2.8731$ $c = 14.1859$	101.41	1.26	0.39	1.91
NC90 0.25 mol% Mo + 0.25 mol% B-doped	$a = 2.8726$ $c = 14.1861$	101.38	1.33	0.41	1.84

agglomerates (secondary particles) comprising submicron primary particles. However, it should be noted that doping results in reduced sizes of primary submicronic particles, for instance, from ~200 to 450 nm in undoped NC90 to ~150 to 250 nm in the Mo-doped sample, as follows from the comparative analysis of the cross-sectional SEM images in Fig. 1f and g. This effect can be ascribed to the so-called induced inhibition of the NC90 particle growth due to the presence of even a small amount of the dopant precursor at the crystallization front during the synthesis[47,48] and agrees with our previous data on doped NCM85 materials.[44]

XRD patterns measured from NC90 undoped and the corresponding doped materials are shown in Fig. 1e, while cell parameters calculated using the Rietveld refinement of these samples are collected in Tables 1 and S2† (calculated by DFT, PBE + U + D3). We indexed all patterns based on the rhombohedral phase Li(TM)O_2 (TM – transition metal) of the layered α-$NaFeO_2$-type structure ($R\bar{3}m$ space group). The calculated XRD peaks intensities ratio $(I_{012} + I_{006})/I_{101}$ (around 0.4) point to a perfect NC90 layered structure with a low degree of mixing with Ni atoms in layers predominantly filled with Li atoms.[49,50] The cell parameters a, c, and their ratio $a/c = 4.94$ almost do not change with doping, while the calculated integral intensity ratio of 003 and 104 peaks I_{003}/I_{104} measure the perfectness of layered NCM materials, increasing with doping. The value $(I_{003}/I_{104}) > 1.2$ indicates a good separation of transition metal ions and Li ions in the respective layers in doped materials. Below, we will discuss cationic Ni^{2+}/Li^+ mixing from the viewpoint of mixing energy E_{mix} and superexchange interactions calculated by DFT (Fig. 3). The lattice parameters obtained from DFT calculations show only minimal changes upon single doping of NC90 with Mo or B, as well as by dual doping with these dopants. It is in line with the experimental data in Table 1. DFT calculations underestimated lattice parameters, as observed in previous studies.[44,51] It could be due to inaccuracies in the DFT method and a lack of inclusion of nuclear thermal effects in the calculations.

TEM analysis of Mo-doped NC90 demonstrates that doping does not change the overall morphology. Regardless of whether a dopant is present or not, the microstructure of the material consists of somewhat elongated grains. However, compared to the undoped material, the grain size in the doped material is noticeably smaller, about 150–200 nm wide.

Analysis of the convergent beam electron diffraction (CBED) patterns obtained from the Mo-doped NC90 material reveals that doping does not cause crystal structure changes compared to the undoped material. Most grains analyzed in TEM were identified as a rhombohedral phase described by the $R\bar{3}m$ space group. Fig. 2a shows an example of the CBED pattern indexed in terms of the Li(TM)O_2 phase. However, in a few cases, grains with the structure assigned to the lithium molybdate Li_2MoO_4 phase (rhombohedral, space group $R\bar{3}$) were observed, as

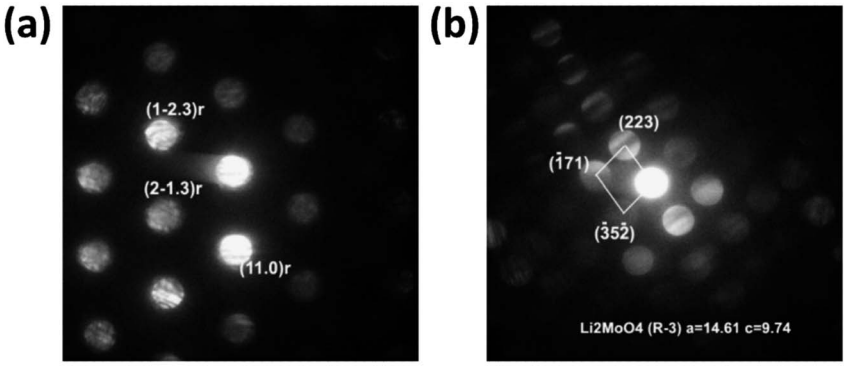

Fig. 2 Examples of electron diffractions taken from Mo-doped NC90 material. (a) CBED pattern indexed in terms of Li(TM)O_2 phase. Label "r" denotes a rhombohedral ($R\bar{3}m$) structure. (b) CBED pattern associated with the Li_2MoO_4 phase.

evidenced by the CBED pattern in Fig. 2b. This phase can be formed during the synthesis of NC90 materials, as it follows from schemes (1) and (3).

To identify the most favorable dopant site in NC90, we computed the formation energy E_f according to eqn (1) and (2), which suggests that for all dopants (*i.e.*, single Mo and B as well as dual Mo–B doping), the Ni-site is preferred over Co and Li sites (Fig. S1†); this is in agreement with previous studies.[44,46,52] Therefore, the following equations were employed for formation energy calculations:

Dopant residing at Ni sites:

$$E_f^{D@Ni} = E(LiNi_{0.9-x}D_xCo_{0.10}O_2) + xE(MO) + 0.00419E(O_2) - E(LiNi_{0.90}Co_{0.10}O_2) - xE(DO) \quad (1)$$

Dopant residing at Li site:

$$E_f^{D@Li} = E(Li_{1-x}D_xNi_{0.90}Co_{0.10}O_2) + \frac{x}{2}E(Li_2O) + 0.00419E(O_2) - E(LiNi_{0.90}Co_{0.10}O_2) - xE(DO) \quad (2)$$

Here, D stands for dopants (Mo, B or Mo–B), $E(LiNi_{0.9-x}D_xCo_{0.1}O_2)$, $E(Li_{1-x}D_xNi_{0.9}Co_{0.1}O_2)$, $E(LiNi_{0.9}Co_{0.1}O_2)$, $E(MO)$, $E(Li_2O)$, $E(DO)$, and $E(O_2)$ are the energies of doped NC90 at Ni or Li sites, undoped NC90, metal oxide (M = Ni or Co), lithium oxide, the dopant in the form of oxide used, and an oxygen molecule, respectively. When B is doped in NC90, DO is B_2O_3, while for Mo-doping, it is MoO_3 per the current work's synthetic procedures. The constant coefficient associated with $E(O_2)$, *i.e.*, 0.00419, is used to balance the equations that may change to dopants concentrations. An equation similar to (1) may be deduced for doping at Co-sites.

In boron-doped NC90, it is evident that B-ions occupy interstitial sites upon geometry optimization due to the relatively shorter bond lengths in B–O.[44] It contributes to a reduced calculated lattice parameter (a = 2.77 Å, Table S2†) for this material. We can conclude from the data obtained that doping does not significantly influence cell characteristics (lattice parameters). At the same time, the calculated X-ray intensity ratios I_{003}/I_{104} and $(I_{012} + I_{006})/I_{101}$ indicate a perfect NC90 structure of both undoped and doped samples and a good separation of Ni^{2+} and Li^+ ions. These ions have comparable sizes of 0.69 Å and 0.76 Å, respectively, which can lead to their mixing,[53] resulting in a less ordered structure. Single doping with molybdenum and dual doping with molybdenum and boron result in slightly improved Ni^{2+}/Li^+ ordering compared to undoped NC90, as follows from higher I_{003}/I_{104} ratios for these samples. Our findings were confirmed by DFT calculations of the Ni^{2+}/Li^+ mixing energy (E_{mix})[54,55] which we defined as the difference between the energy of layered NC90 (undoped and doped) structure and Ni^{2+}/Li^+ inter-mixed NC90 (undoped and doped). Lower E_{mix} values indicate more favorable Ni^{2+}/Li^+ cation mixing. DFT results show (Fig. 3) that the E_{mix} of doped NC90 materials is higher than that of undoped (pristine) NC90: NC90 = 1.45 eV; Mo-doped NC90 = 2.18 eV; Mo–B-doped NC90 = 1.98 eV; B-doped NC90 = 1.76 eV, suggesting there will be lesser mixing in the doped materials. We note that the current findings are in contradiction to the recent work of Sun *et al.*[55]

To further rationalize the obtained mixing energies, we analyzed the spin orientations of Ni atoms and their local arrangement in undoped (pristine) and doped NC90 with and

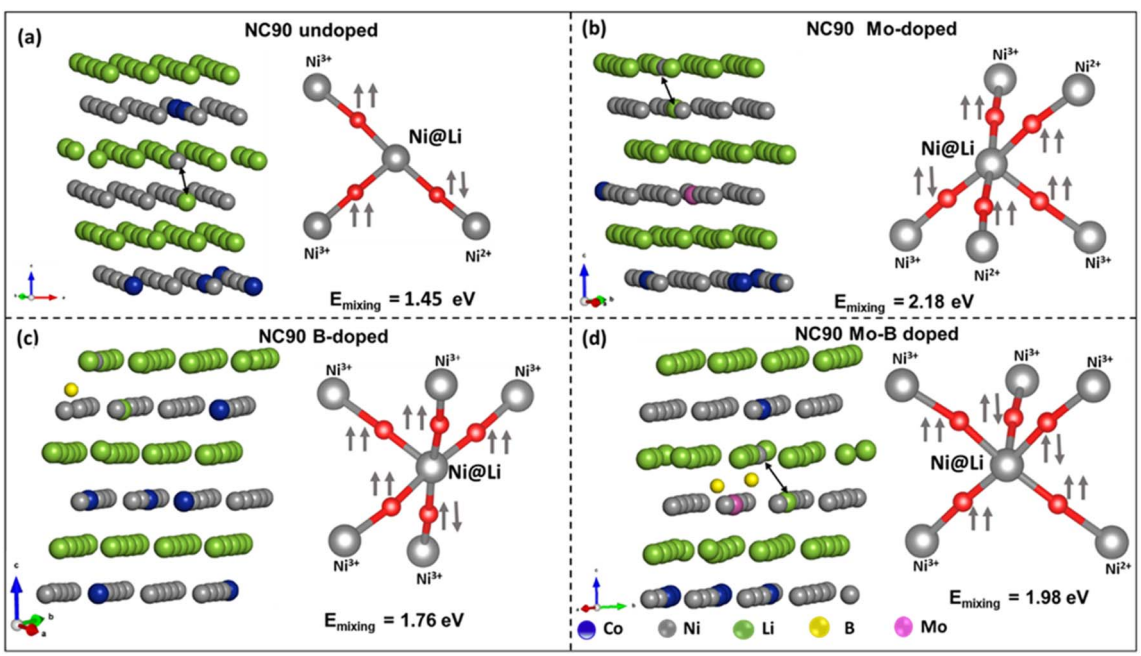

Fig. 3 Crystal structures and spin orientation of nearest Ni-ions upon Ni^{2+}/Li^+ interlayer mixing of undoped NC90 material (a) and those of single-doped with molybdenum (b), single-doped with boron (c) and dual-doped with these dopants (d), calculated by DFT. Values of mixing energy E_{mix} of the above materials are indicated. Note: black arrows indicate the Ni-ions in the Li-layer.

without Ni^{2+}/Li^{+} interlayer mixing. Ideally, Ni^{2+}/Ni^{3+} ions in the TM layer form 90° intra-layer, superexchange environments with their neighboring TMs *via* O^{2-} due to their unpaired d-electrons. Upon Ni^{2+}/Li^{+} mixing, Ni^{2+} ions in the Li-layer might form 180° superexchange interactions *via* O^{2-} with other TM-ions in the TM layers. The strongest superexchange interactions occur for Ni^{2+}–O–Ni^{2+} linear arrangements, due to $e_g(\uparrow\uparrow)$–$(\downarrow)2p(\uparrow)$–$e_g(\downarrow\downarrow)$ electron interactions, while Ni^{2+}–O–Ni^{3+} arrangements are weaker, due to $e_g(\uparrow\uparrow)$–$(\downarrow)2p(\uparrow)$–$e_g(\downarrow)$ electron interactions.[32,56] Higher E_{mix} implies that cation mixing is less favorable (*i.e.*, the possible absence of Ni^{2+}–O–Ni^{2+} linear arrangements with anti-parallel spins). Indeed, we may attribute higher values of E_{mix} to the absence of Ni^{2+}–O–Ni^{2+} linear sequences with anti-parallel spins.[32] Hence, a lack of superexchange interactions, as the spin orientation of Ni@Li (Ni^{2+} mixed into Li^{+} layer) and nearest neighbor Ni-ions are mostly parallel (Fig. 3). It agrees with our experimental observations of intensity ratios of 003/104 peaks obtained from the XRD profiles (Table 1), where this ratio for doped NC90 is greater than 1.2.[46] Conclusively, single doping of NC90 with Mo, B, and dual Mo–B modification form more stable structures without significant cation mixing, resulting in improved electrochemical performance as cathodes in Li-battery systems, higher discharge capacities, and steady cycling behavior.

To further validate our cation mixing results, we analyzed the crystal orbital Hamiltonian population (COHP) for Ni^{2+}/Li^{+} inter-mixed NC90 (undoped and doped systems) shown in Fig. S2.† It is evident from Fig. S2† that the value of the absolute integrated COHP (ICOHP) for Ni–O in undoped NC90 is greater than the ICOHP (Ni–O) of its doped counterpart (including Ni^{2+}/Li^{+} mixing), suggesting that Ni^{2+}/Li^{+} mixing results in weaker Ni–O bonding. Furthermore, it indicates that cation mixing is unfavorable in doped NC90 materials.

2.2 Electronic structure and distribution of Ni-ions in NC90 materials

It is important to understand the electronic structure and redox activity of each elemental species of undoped and doped NC90. The total and partial densities of states (DOS) of NC90 undoped and doped samples are shown in Fig. 4a–d.

A small energy gap is observed for all systems except for Mo-doped NC90. A significant orbital mixing of Ni-3d and O-2p states was observed near the Fermi level in the undoped NC90 material (Fig. 4a), along with some Co-3d states. Inspection of the partial DOS indicates that Ni^{2+} states dominate the valence band (VB), suggesting that Ni-ions are the predominant redox active species in undoped NC90. These ions will be oxidized first upon charging the cathode in Li-cells. Asymmetric spin channels (up and down) are observed in Ni^{2+} and Ni^{3+} states, while the spin channels are symmetric for Ni^{4+} and Co^{3+} states. We note that asymmetric spin channels yield high-spin (HS) states while symmetric spin channels give low-spin (LS) states. Thus, in undoped NC90, Ni^{2+} and Ni^{3+} states are HS species, while Ni^{4+} and Co^{3+} are in LS states. The partial DOS for Mo-doped

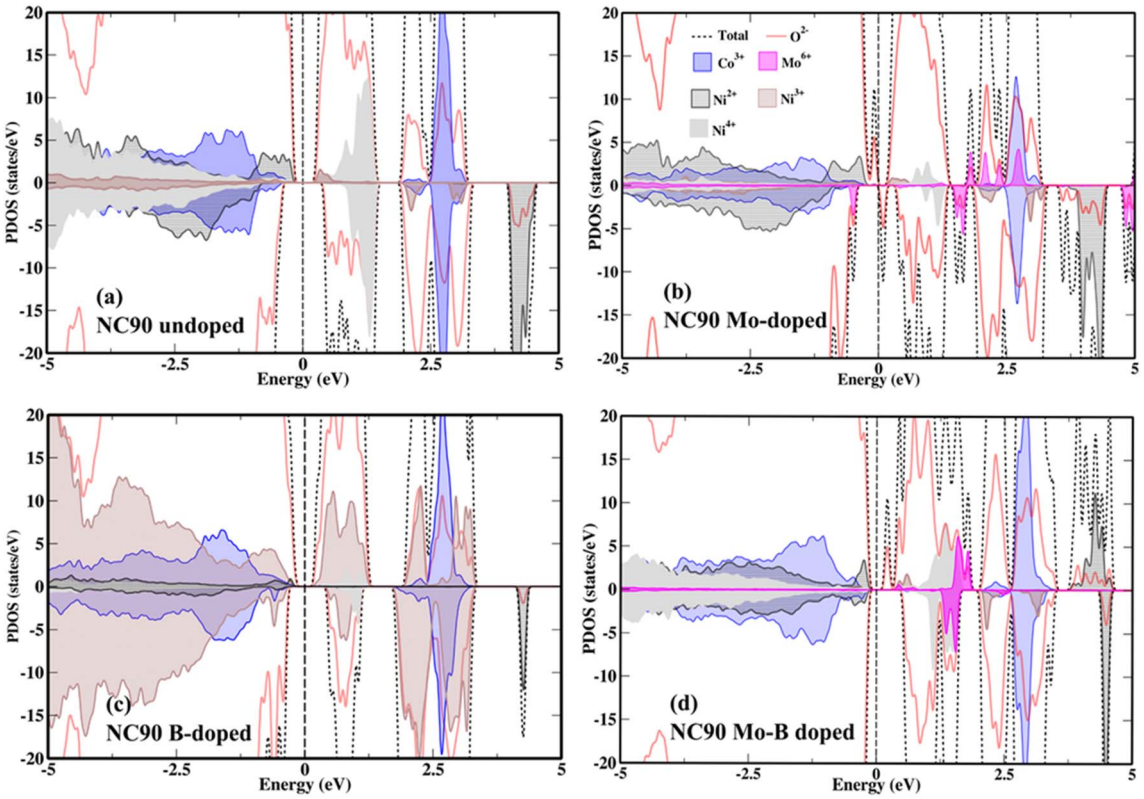

Fig. 4 DOS and PDOS of (a) undoped NC90 and (b) Mo-doped, (c) B-doped, and (d) Mo–B dual-doped materials. The favorable site of the dopant is Ni-site in NC90. The Fermi level is set at 0.0 eV.

NC90 is shown in Fig. 4b. Also, Ni^{2+} and Ni^{3+} are in HS states, while Ni^{4+} and Co^{3+} are in LS states. Seemingly, Mo^{6+} is slightly spin-polarized, which could indicate some reduction. Mo, in a high valence state (+6), introduces more electrons into the system, helps reduce interfacial charge-transfer resistance, and improves electronic conductivity.[45,46] Mo introduces numerous additional Mo-4d states in the conduction band (CB), which facilitates charge transfer (Fig. 4b and d), in agreement with our previous reports.[46,52] A significant spread of Ni^{3+} states can be seen in Fig. 4c, while low spectral intensity peaks are observed for Ni^{2+} states. B-2p states are not found near Fermi level.[44] Ni^{2+} and Ni^{3+} states are present in HS, whereas Ni^{4+} and Co^{3+} are all in LS states (Fig. 4c).[44] Ni^{2+} and Co^{3+} states are observed near the Fermi level in the VB region, while a small peak of Ni^{3+} states is seen in the CB near the Fermi level. The partial DOS of dual-doped NC90 with Mo–B is shown in Fig. 4d, which shows that Ni^{2+} states are located in the VB, while some Mo-4d states are observed in the CB, along with low-intensity Ni^{3+} states. Ni^{2+} and Ni^{3+} states are present in HS, while Mo^{6+}, Ni^{4+}, and Co^{3+} states are in LS.

To analyze the effect of doping in NC90 on the distribution of Ni-ions in different oxidation states (Ni^{2+}, Ni^{3+}, and Ni^{4+}), we calculated the magnetic moments per Ni-site, as the oxidation states of Ni-ions are characterized by magnetic moment per Ni-ion.[57–59] The distribution of Ni-ions in undoped and doped NC90 is given in Fig. S3.† The moments for Ni^{2+}, Ni^{3+}, and Ni^{4+} were calculated to be *ca.* 2 μ_B, 1 μ_B, and 0 μ_B, respectively. Upon doping, the variation in oxidation states of Ni-ions is attributed to maintaining charge neutrality by charge-redistribution. Upon B-doping, the concentrations of Ni^{2+} and Ni^{4+} ions are significantly reduced while Ni^{3+} becomes the dominant species. In Mo-doped NC90, the concentration of Ni^{2+} ions is higher by ~2.2 times compared to the undoped material, while the concentrations of Ni^{3+} and Ni^{4+} ions are significantly reduced. In Mo–B-doped NC90, Ni^{2+} ions are more abundant than in undoped NC90, and there are also more Ni^{3+} ions in Mo–B-doped NC90 than in the undoped one. Our calculated Ni-ions populations agree well with the experimental XPS data in Fig. S4.† Indeed, these XPS studies (though related mostly to the surface of NC90 samples) and the corresponding calculations demonstrate, for instance, that in the Mo-doped NC90, the Ni^{2+} content is higher by ~3 times compared to that in the undoped one. Spectroscopic results also show that Ni^{2+} increased by a factor of ~2 in the Mo–B double-doped material; this is in good correlation with the model of the Ni-ions population in Fig. S3.†

To further verify our findings regarding the stability of undoped and doped NC90 in terms of possible oxygen evolution, we performed COHP calculations, which provide information regarding metal–oxygen bonding (Fig. S5†). A more negative integrated COHP (ICOHP) is indicative of stronger bonding. Undoped (Fig. S5a†) and doped NC90 (Fig. S5b and d†) do not significantly affect the bond strength of Ni–O and Co–O. However, the ICOHP of Mo–O in Mo-doped (Fig. S5b†), B–O in B-doped (Fig. S5c†), and Mo–O and B–O in dual Mo–B-doped (Fig. S5d†) NC90 models exhibit stronger bonding. Such strong bonding implies that B and Mo dopants can prevent, to some extent, lattice oxygen evolution.[44,52,60,61]

2.3 Electrochemical behavior of NC90 cathodes in half Li-cells and full cells with graphite anodes

We studied the cycling performance of undoped and single Mo, B, and dual Mo–B doped cathodes *vs.* Li-counter electrodes in half-cells and graphite anodes in full cells using coin-type and pouch-type configurations, respectively.

Fig. 5 exhibits smooth charge–discharge voltage profiles of the 1st cycle in a 3.0–4.3 V range (C/10 rate, 25 °C) of these electrodes in coin-type cells. The calculated voltage curves obtained from DFT studies (PBE + D3 and rigidly shifted by 0.8 eV) are shown in Fig. 5b, demonstrating good agreement with the experimental profiles. These profiles are typical for Ni-rich NCM electrodes in EC-EMC/$LiPF_6$-based solutions exhibiting short voltage plateaus at ~4.2 V, ascribed in the literature to structural phase transitions of the coexisting hexagonal phases (H2 + H3) to H3.[62,63] An overvoltage of ~100 mV measured during the charge at ~3.7 V of undoped and B-doped NC90 electrodes can be attributed to some resistance due to remaining surface impurities (LiOH, Li_2CO_3), boron-containing species, like Li_3BO_3. This overvoltage usually disappears upon further cycling during the second charging and subsequent cycles (Fig. 5c). The irreversible capacity losses of undoped, Mo, B and Mo–B doped electrodes were calculated to be 10.5, 10.6, 11.6, and 11.5%, as averaged from three galvanostatic charge–discharge tests, for statistical purposes. Although undoped samples deliver slightly higher discharge capacity in the 1st cycle (~215 mA h g^{-1} compared to 213, 213, and 210 mA h g^{-1}, respectively, for Mo, B, and dual doped cathodes), those delivered by Mo, B, and Mo–B doped electrodes upon further cycling are much higher as demonstrated in Fig. 5c and d. These doped NC90 cathodes display higher capacities upon prolonged cycling in lithium half-cells and full-cells with graphite anodes, Fig. 6a and c, respectively. We suggest that enhanced discharge capacities can be explained by a higher content of the electrochemically active Ni^{2+} ions, for instance, in Mo and Mo–B doped NC90. It follows from our calculations of Ni-ion concentrations in undoped and doped samples (Fig. S3†). Note that surface-sensitive XPS studies in Fig. S4† indicate a higher amount of divalent nickel in doped materials. As expected, we have measured a remarkably increased of up to 95% capacity retention (expressed as the ratio of capacities obtained at 100th and 24th cycles, Q_{100}/Q_{24}) of the corresponding Mo-doped electrodes compared to undoped ones (only 70–76%) cycled *vs.* Li-metal and *vs.* graphite anodes, respectively. Doped cathodes (mainly those with Mo and Mo–B dually doped) also deliver higher discharge capacities, enhanced capacity retention at various rates (Fig. S6†), higher energy densities around 700–770 W h kg^{-1} (Fig. S7†), and much lower voltage hysteresis. This parameter was calculated as the difference between the mean voltage in charge and discharge (Fig. 6b). We attribute these results to more stable structures of doped cathodes due to the higher Ni^{2+}/Li^{+} mixing energy of these samples in agreement with our conclusion from DFT studies of crystal structures and

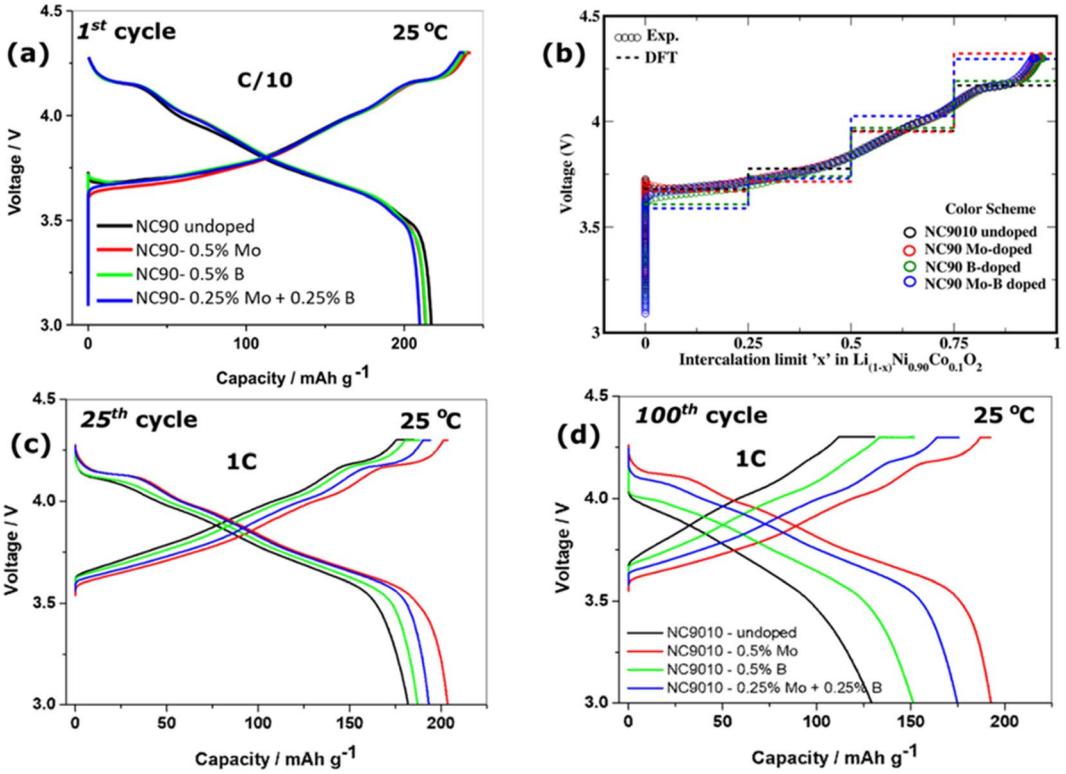

Fig. 5 (a, c and d) Charge–discharge voltage profiles of the 1st cycle in a 3.0–4.3 V range of NC90 undoped and doped electrodes (as indicated) tested in coin-type cells with LP57 solutions (C/10 rate, 25 °C). (b) The calculated voltage profiles obtained from DFT studies (PBE + D3) demonstrated good agreement with the experimental data.

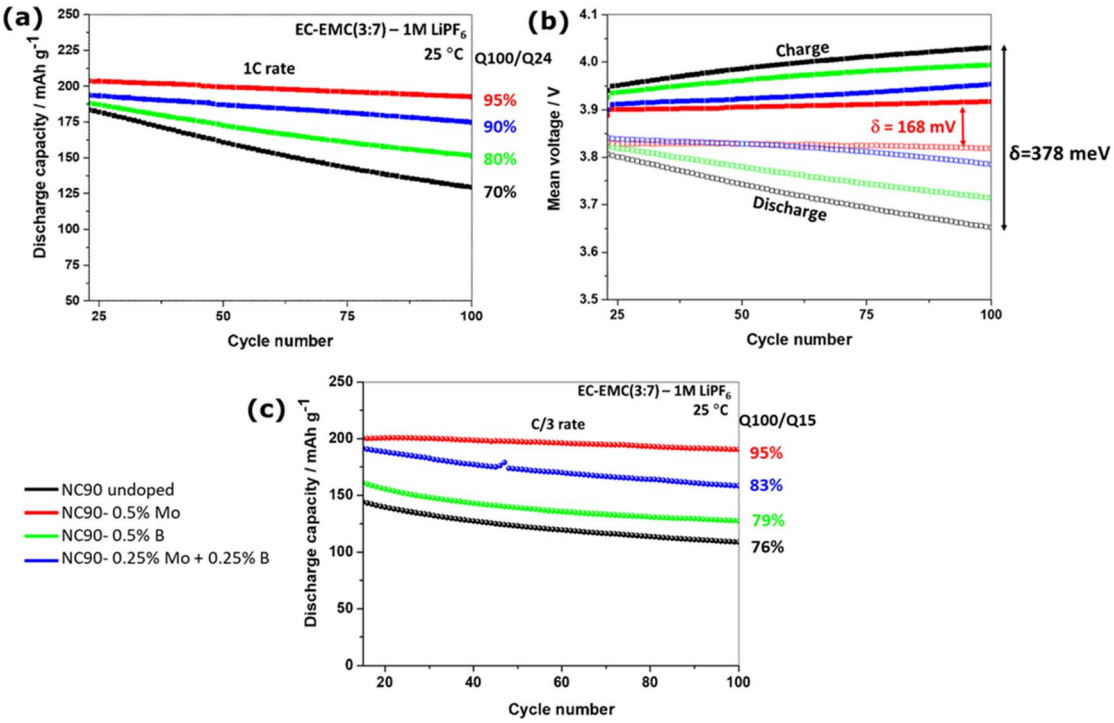

Fig. 6 (a) and (c), respectively, show the cycling behavior of electrodes comprising NC90 undoped and doped materials, as indicated, in half-cells *vs.* lithium anodes (1C rate) and full-cell *vs.* graphite anodes (C/3 rate, LP57 solutions). Capacity retentions (Q) are indicated as ratios of capacities delivered in cycles 100th and 24th (a), and 15th (c). The potential range was 3.0–4.3 V at 25 °C. (b) Demonstrates mean voltage profiles measured from the above electrodes.

spin orientation of nearest Ni-ions upon Ni^{2+}/Li^{+} interlayer mixing (Fig. 3), as well as strong dopant-oxygen bonds.

We have also established that doped electrodes exhibited lower interfacial charge-transfer resistance R_{ct} calculated from impedance spectra than their undoped counterparts (Table S3†). Impedance spectra of NC90 electrodes (Fig. S8a and b†) measured at 4.0 V after the 10th and 50th cycles were typical for NCM cathodes and similar to those presented in our previous reports on undoped and Zr-doped NCM622 electrodes[64] and NCM811 and NCM85 cathodes single doped by Mo and B.[44–46] These experimental observations of lower R_{ct} for doped cathodes correlate well with our suggestion that Mo^{6+} doping introduces more electrons into the system and induces, thus, the formation of additional conduction bands near the Fermi level (Fig. 4b and d). Moreover, we propose that a new phase Li_2MoO_4 (lithium molybdate) formed upon synthesizing the Mo and Mo–B-doped samples (schemes (1) and (3)) contributes to modifying the electrode/solution interface of NC90 cathodes due to its tunnel structure and electrochemical activity in Li-cells.[65–67] Therefore, lower charge transfer resistance and higher exchange current facilitate ion and electron transport at the interface of doped electrodes, similar to that in NCM85 Mo-doped materials.[45] Decreasing the charge-transfer resistances measured from NC90 cycled electrodes dually doped with Mo and B can be explained by a synergistic effect where both dopants modify the electrode/solution interface, as follows: Mo^{6+} contributes by the formation of a new conduction band near the Fermi level and a new Li-conducting phase of Li_2MoO_4. At the same time, due to the B^{3+} dopant, ion-conductive surface species Li_3BO_3 were formed, which are known to promote Li^{+} interfacial transport.[62] Faster electrochemical kinetics of doped NC90 cathodes is illustrated by the differential capacity (dQ/dV) *vs.* potential (V) plots of these electrodes in Fig. 7. Indeed, Mo and B single-doped and Mo–B dual-doped samples exhibit sharp anodic and cathodic peaks, and much lower potential differences Ean – Ecath compared to the undoped NC90 (Table S4†). Notably, oxidation peaks recorded at around 4.2 V and related to the structural transition of H2 + H3 hexagonal phases to H3 at the end of charging, reflect higher reversibility in the doped cathodes, implying thus enhanced structural stability, in line with literature reports.[37,46,52]

Interestingly, we observe that boron segregates at the surface of NC90, similarly to that in the related Ni-rich material comprising 85 at% Ni.[44] Fig. S9† illustrates the segregation (depth) profile of the B^{3+} dopant in NC90 measured by ToF-SIMS and indicates that the "outermost surface layer" of ~30 Å is enriched with boron. Note this profile represents an average from several similar measurements of NC90 samples doped only with boron and those dually doped with B^{3+} and Mo^{6+}. Inserts to Fig. S9† are 3D renders of B, Mo, and both dopants (Mo–B) exhibiting, respectively, enrichment of the surface layer with boron and a homogeneous distribution of boron and molybdenum on the surface and in the bulk of the corresponding NC90 samples. We note that the 3D render overlay of B and Mo in this figure exhibits both partial segregations of boron to the surface and distribution of the dopants in bulk. The homogenous dispersion of Mo throughout the particles is somewhat puzzling as in the similar material NCM85, and we observed that Mo segregates at the surface.[46]

To better understand the Mo surface segregation phenomenon, we modeled the NC90 surface with eight atomic layers (48 formula units) in the (104) surface plane, as it is a non-polar and stable plane,[18,44] and this plane allows Li conductivity. We calculated the surface energy difference $\Delta\gamma = \gamma_{undoped} - \gamma_{doped}$ (meV per A^2 per atom) for undoped and doped samples corresponding to 1.66 mol% (Table S5†). To determine the preferred position of a dopant (for instance, molybdenum), we substituted a Ni-ion with a Mo-ion at the top and in the middle of the slab, respectively, as shown in Fig. S9b.† Our computational results demonstrate the energy preference for doping at the surface relative to bulk (*i.e.*, in the middle of the slab). For instance, Mo prefers surface segregation by 3.37 eV. For a clear

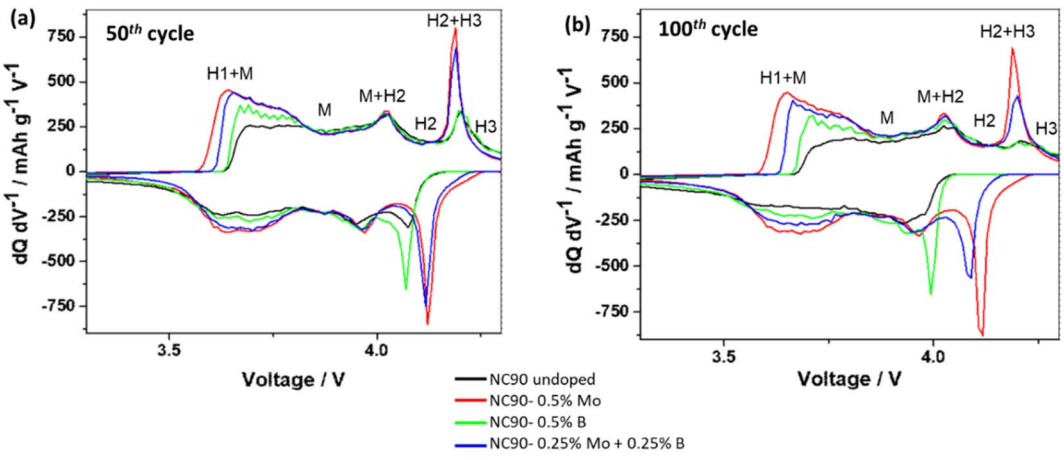

Fig. 7 Differential capacity (dQ/dV) *vs.* potential (V) plots of electrodes comprising NC90 undoped and doped materials, as indicated, measured at cycle 50th (a) and 100th (b) in half-cells *vs.* lithium anodes (LP57 solutions, 1C rate, 25 °C). Indicated are hexagonal H and monoclinic M phases and their possible multistep structural transitions in NC90 electrodes upon charge/discharge, as it is well established in the literature (see, for instance: refs. [18], 68, 39 and 44).

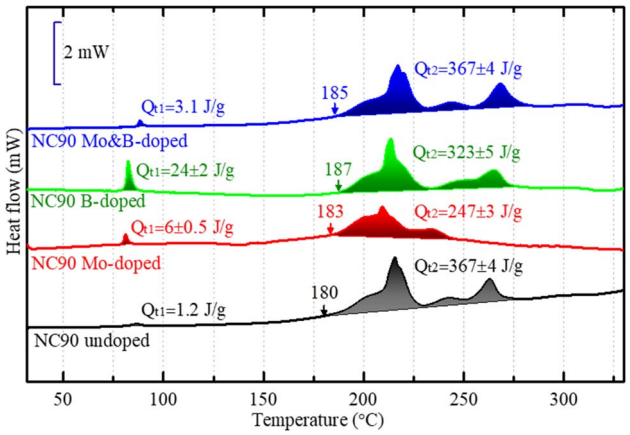

Fig. 8 DSC profiles of electrodes comprising NC90 undoped and doped materials terminated in a charged state of 4.3 V during the 1st cycle in half coin-type *vs.* lithium anodes.

understanding of the effect of dopant concentration on the surface segregation phenomenon, we performed a comparative analysis with different doping concentrations. Specifically, we extended the unit cell by increasing it with 768 atoms (modeling ~0.5 mol% Mo-dopant concentration). To model the even lower B and Mo concentration of 0.25 mol% used in the dual-doped samples, we included 960 atoms in the unit cell. The surface energy differences per atom between the undoped and the singly Mo-doped and the dually B and Mo-doped NC90 decrease with a lowering dopant concentration of Mo or B (Table S5†). Therefore, we can qualitatively conclude that surface segregation decreases with decreasing dopant concentration. Indeed, segregation is less pronounced in the case of dually Mo and B doped NC90 with half the concentration (0.25 mol%) of each dopant compared to single-doping samples.

Based on the DSC profiles of the electrodes, we can draw an additional important conclusion from our study, namely that Mo-doped electrodes (in the charged state at 4.3 V) were found to be more stable in thermal interactions with EC-EMC/$LiPF_6$ solutions demonstrating much lower heat evolution Q_{T2} compared to undoped NC90 (Fig. 8). Since this exothermic heat is commonly associated with reactions of the lattice oxygen and solution species, we assume less O_2 is released from doped electrodes in the charged state. This correlates well with the conclusion on stronger metal-O bonds (Ni–O) made from the corresponding ICOHP calculations (see discussion of Fig. S5† above), implying that stronger bonding prevents, in part, lattice oxygen release upon charging of NC90 doped electrodes. Interestingly, the heat evolution Q_{T1} at around 85 °C due to the surface interactions of B-doped materials with solution species is much higher than that for the undoped samples (Fig. 8). This is likely because along with surface Li_2CO_3 formed on the material upon contact with air, and LiOH remaining from the synthesis, some newly formed B-containing species, like Li_3BO_3, $Ni_3(BO_3)_2$ also interact at the surface and contribute to the heat evolved from thermal reactions.[44]

2.4 Post-cycling structural analysis of NC90 cathodes

We have established a correlation between the electrochemical performance of NC90 electrodes and their microstructural deteriorations caused by cycling. Undoped NC90 electrodes demonstrate severe capacity fading in coin-type Li-cells and full pouch-cells (Fig. 6), resulting in substantial structural changes in the electrodes. It is shown by cross-sectional images of these samples in Fig. 9a and c.

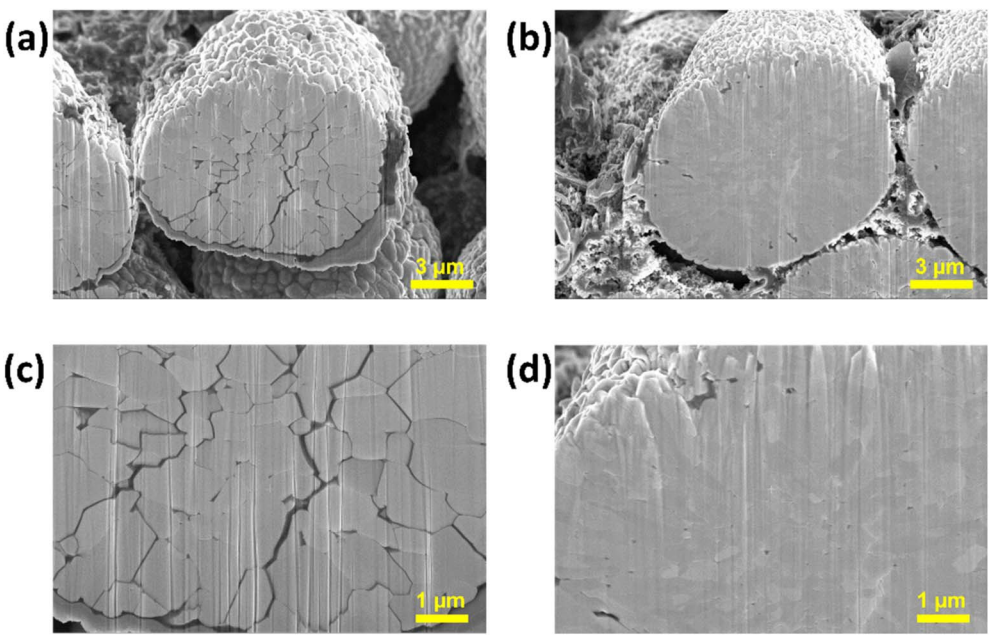

Fig. 9 FIB cross-sectional images of NC90 undoped (a and c) and Mo-doped (b and d) electrodes terminated in the discharge state after cycling 50 times at a C/3 rate (25 °C).

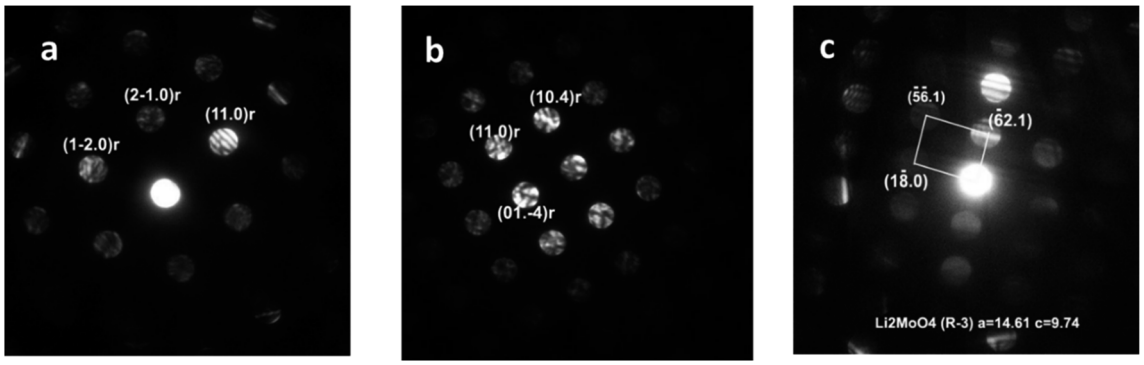

Fig. 10 CBED patterns taken from cycled NC90 electrodes (50 cycles at a C/3 rate, 25 °C). (a) The pattern is indexed based on the rhombohedral Li(TM)O_2 phase labeled "r" in undoped cycled material. (b) and (c) Mo-doped cycled material. Pattern (b) is indexed in terms of the Li(TM)O_2 phase, and pattern (c) corresponds to Li_2MoO_4 rhombohedral phase.

The secondary particles of undoped NC90 material are disintegrated and possess an extended network of deep cracks among the primary particles (grains). Such cracks are partly the reason for capacity fading as the electrolyte solution can penetrate through the cracks, deep into the particle's interior, causing side reactions and allowing further structural and morphological destruction of the active material.[38] In contrast, Mo-doped samples reveal good capacity retention of 95%, and their secondary particles remain intact and integrated, showing no cracks (Fig. 9b and d). It may be further explained by the smaller grains and more closely integrated particles in the Mo-doped material relative to the undoped one (Fig. 1f and g). It agrees with literature reports that Mo-dopant can refine and suppress grain and particle growth.[69,70] Our TEM studies of the cycled doped and undoped NC90 materials show no noticeable changes in the grain morphology and crystallographic structure. The grain size is about 400–450 nm and 150–200 nm, as in the uncycled undoped and Mo-doped materials, respectively, and the rhombohedral structure attributed to the Li(TM)O_2 phase remains unchanged (Fig. 10a and b).

A new phase of lithium molybdate Li_2MoO_4 (rhombohedral, space group $R\bar{3}$) formed upon the synthesis of doped NC90 is retained during prolonged cycling, as confirmed by diffraction patterns in Fig. 10c. Furthermore, it indicates that surface Li_2MoO_4 species contribute to modifying the interface of NC90 cathodes, enhancing the electrochemical performance (decreased charge-transfer resistance and faster kinetics) of doped samples, as discussed above.

3. Conclusions

This work successfully synthesized the high-nickel, low-cobalt layered cathode material $LiNi_{0.9}Co_{0.1}O_2$ and its modified analogs: singly doped with Mo^{6+} and B^{3+} and as well as dually doped with these cations. Analysis of XRD patterns of the above materials allowed us to conclude that there is a good separation of transition metal ions (especially Ni^{2+} and Li^+) into their corresponding layers. Based on DFT mixing energy calculations, we conclude that Ni^{2+}/Li^+ cation mixing is not favorable in doped NC90, thanks to the effect of the dopants on the electronic properties of the materials. Computed formation energies indicate that the dopants prefer Ni-site substitution over Co and Li sites for all the dopants (*i.e.*, single Mo and B and dual Mo–B doping).

We further demonstrated that doping $LiNi_{0.9}Co_{0.1}O_2$ results in stable electrochemical performance in half-cells and full-cells *vs.* lithium and graphite anodes, respectively. Typically, stabilized cathodes doped with Mo or dual Mo–B doped exhibit much higher capacity retention (by 20–25%), half the voltage hysteresis, and substantially decreased interfacial charge-transfer resistance R_{ct} calculated from impedance measurements during cycling. This improved electrochemical cycling behavior of doped NC90 can be attributed to more stable structures of doped cathodes due to higher Ni^{2+}/Li^+ mixing energy in these samples. Lower R_{ct} is explained by the formation of additional conduction bands near the Fermi level resulting in a higher exchange current. Moreover, lithium molybdate Li_2MoO_4 – a new phase formed upon the synthesis of doped NC90 and preserved during prolonged cycling, also contributes to modifying the interface of cathodes due to its tunnel structure and electrochemical activity with lithium. We suggest that decreased R_{ct} and faster electrochemical kinetics measured from Mo–B dual-doped electrodes can be attributed to a synergistic effect of these dopants: Mo^{6+} contributes by the formation of a new conduction band near the Fermi level and a new Li-conducting phase of Li_2MoO_4, while the B^{3+} dopant forms the ion-conductive surface species Li_3BO_3, promoting Li^+ interfacial transport.

The structural and chemical stability of the doped NC90 cathodes was rationalized based on strong Mo–oxygen and B–oxygen bonding in the doped materials, using ICOHP calculations. It implies that dopants can prevent, to some extent, lattice oxygen evolution and stabilize these high-Ni electrodes upon charging to 4.3 V. Furthermore, we observed less evolved heat upon reactions of the doped samples in the charged state (4.3 V) with battery solutions in DSC studies. We conclude that the particles of cycled Mo-doped NC90 cathodes retain the integrity and microstructural stability (*i.e.*, no cracks were formed), in contrast to undoped particles that exhibit significant structural degradation with a network of cracks. It correlates well with the

more stable and reversible electrochemical behavior of doped samples especially upon charging in the potential domain of 4.2–4.3 V corresponding to an H2 + H3 → H3 phase transition, in agreement with previous reports.

We emphasize the coherence of all the experimental results we obtained. The doped materials outperform the reference undoped NC90 cathode material, while the best electrochemical performance was obtained with Mo-doped NC90 and dually B and Mo-doped NC90 material. This order of improved performance is fully correlated with lower impedance, lower heat evolution in thermal reactions of charged cathode materials with standard electrolyte solutions, and higher structural stability demonstrated in post-mortem analyses of cycled electrodes. The dual doping may deserve further optimization work since we assume that doping by several cations may have important synergistic effects. In addition, the current work can inspire further theoretical and experimental studies that will determine whether atomic vacancies are created due to doping by heteroatoms in lithiated transition metal cathode materials.

In summary, we anticipate that this work can play a role in a further improved design of Ni-rich high-energy layered-structure electrodes for advanced lithium-ion batteries.

Author contributions

Francis Amalraj Susai: conceptualization, synthesis of materials and characterization, data curation, writing a draft. Amreen Bano and Arup Chakraborty: methodology, computational modeling and calculations, data curation, discussion and writing a draft. Sandipan Maiti: surface characterization by XPS and thermal studies; Judith Grinblat: microscopic studies, writing original draft preparation. Hadar Sclar and Tatyana Kravchuk: surface characterization by XPS and ToF-SIMS, data curation; Aleksandr Kondrakov: materials synthesis, discussion, funding, Maria Tkachev: microscopic studies. Michael Talianker: structural analysis by XRD, TEM, and electron diffraction, discussion, writing original draft preparation. Dan Thomas Major: conceptualization, methodology, DFT calculations, discussion, writing and editing the original draft. Boris Markovsky: conceptualization, methodology, electrochemical studies, discussion, writing and editing the original draft. Doron Aurbach: conceptualization, writing original draft preparation, editing, discussion, funding.

Conflicts of interest

The authors declare no conflict of interest.

References

1 C. P. Grey and D. S. Hall, Prospects for lithium-ion batteries and beyond—a 2030 vision, *Nat. Commun.*, 2020, **11**(1), 6279.
2 J. Jyoti, B. P. Singh and S. K. Tripathi, Recent advancements in development of different cathode materials for rechargeable lithium ion batteries, *J. Energy Storage*, 2021, **43**, 103112.
3 W. Li, E. M. Erickson and A. Manthiram, High-nickel layered oxide cathodes for lithium-based automotive batteries, *Nat. Energy*, 2020, **5**(1), 26–34.
4 A. Chakraborty, S. Kunnikuruvan, S. Kumar, B. Markovsky, D. Aurbach, M. Dixit and D. T. Major, Layered cathode materials for lithium-ion batteries: review of computational studies on $LiNi_{1-x-y}Co_xMn_yO_2$ and $LiNi_{1-x-y}Co_xAl_yO_2$, *Chem. Mater.*, 2020, **32**(3), 915–952.
5 F. A. Susai, H. Sclar, Y. Shilina, T. R. Penki, R. Raman, S. Maddukuri, S. Maiti, I. C. Halalay, S. Luski, B. Markovsky and D. Aurbach, Horizons for li-ion batteries relevant to electro-mobility: high-specific-energy cathodes and chemically active separators, *Adv. Mater.*, 2018, **30**(41), 1801348.
6 J. Hu, F. Fan, Q. Zhang, S. Zhong and Q. Ma, Effects of long-term fast charging on a layered cathode for lithium-ion batteries, *J. Energy Chem.*, 2022, **67**, 604–612.
7 F. Wu, N. Liu, L. Chen, N. Li, J. Dong, Y. Lu, G. Tan, M. Xu, D. Cao, Y. Liu, Y. Chen and Y. Su, The nature of irreversible phase transformation propagation in nickel-rich layered cathode for lithium-ion batteries, *J. Energy Chem.*, 2021, **62**, 351–358.
8 T.-F. Yi, J. Mei and Y.-R. Zhu, Key strategies for enhancing the cycling stability and rate capacity of $LiNi_{0.5}Mn_{1.5}O_4$ as high-voltage cathode materials for high power lithium-ion batteries, *J. Power Sources*, 2016, **316**, 85–105.
9 J. Ma, P. Hu, G. Cui and L. Chen, Surface and interface issues in spinel $LiNi_{0.5}Mn_{1.5}O_4$: insights into a potential cathode material for high energy density lithium ion batteries, *Chem. Mater.*, 2016, **28**(11), 3578–3606.
10 L. Liang, W. Zhang, F. Zhao, D. K. Denis, F. U. Zaman, L. Hou and C. Yuan, Surface/interface structure degradation of Ni-rich layered oxide cathodes toward lithium-ion batteries: fundamental mechanisms and remedying strategies, *Adv. Mater. Interfaces*, 2020, **7**(3), 1901749.
11 W. Li, B. Song and A. Manthiram, High-voltage positive electrode materials for lithium-ion batteries, *Chem. Soc. Rev.*, 2017, **46**(10), 3006–3059.
12 A. Manthiram, J. C. Knight, S.-T. Myung, S.-M. Oh and Y.-K. Sun, Nickel-rich and lithium-rich layered oxide cathodes: progress and perspectives, *Adv. Energy Mater.*, 2016, **6**(1), 1501010.
13 V. Etacheri, R. Marom, R. Elazari, G. Salitra and D. Aurbach, Challenges in the development of advanced Li-ion batteries: a review, *Energy Environ. Sci.*, 2011, **4**(9), 3243–3262.
14 R. Schmuch, R. Wagner, G. Hörpel, T. Placke and M. Winter, Performance and cost of materials for lithium-based rechargeable automotive batteries, *Nat. Energy*, 2018, **3**(4), 267–278.
15 F. Schipper, E. M. Erickson, C. Erk, J.-Y. Shin, F. F. Chesneau and D. Aurbach, Review—recent advances and remaining challenges for lithium ion battery cathodes, *J. Electrochem. Soc.*, 2017, **164**(1), A6220.
16 W. Liu, P. Oh, X. Liu, M.-J. Lee, W. Cho, S. Chae, Y. Kim and J. Cho, Nickel-rich layered lithium transition-metal oxide for high-energy lithium-ion batteries, *Angew. Chem., Int. Ed.*, 2015, **54**(15), 4440–4457.

17 J. Lai, J. Zhang, Z. Li, Y. Xiao, W. Hua, Z. Wu, Y. Chen, Y. Zhong, W. Xiang and X. Guo, Structural elucidation of the degradation mechanism of nickel-rich layered cathodes during high-voltage cycling, *Chem. Commun.*, 2020, **56**(36), 4886–4889.

18 K.-J. Park, H.-G. Jung, L.-Y. Kuo, P. Kaghazchi, C. S. Yoon and Y.-K. Sun, Improved cycling stability of $Li[Ni_{0.90}Co_{0.05}Mn_{0.05}]O_2$ through microstructure modification by boron doping for li-ion batteries, *Adv. Energy Mater.*, 2018, **8**(25), 1801202.

19 S.-M. Bak, E. Hu, Y. Zhou, X. Yu, S. D. Senanayake, S.-J. Cho, K.-B. Kim, K. Y. Chung, X.-Q. Yang and K.-W. Nam, Structural changes and thermal stability of charged $LiNi_xMn_yCo_zO_2$ cathode materials studied by combined *in situ* time-resolved XRD and mass spectroscopy, *ACS Appl. Mater. Interfaces*, 2014, **6**(24), 22594–22601.

20 F. Lin, I. M. Markus, D. Nordlund, T.-C. Weng, M. D. Asta, H. L. Xin and M. M. Doeff, Surface reconstruction and chemical evolution of stoichiometric layered cathode materials for lithium-ion batteries, *Nat. Commun.*, 2014, **5**(1), 3529.

21 H.-H. Ryu, K.-J. Park, C. S. Yoon and Y.-K. Sun, Capacity fading of Ni-rich $Li[Ni_xCo_yMn_{1-x-y}]O_2$ ($0.6 \leq x \leq 0.95$) cathodes for high-energy-density lithium-ion batteries: bulk or surface degradation?, *Chem. Mater.*, 2018, **30**(3), 1155–1163.

22 J. C. Luo, J. F. Luo, C. L. Chen, W. H. Huang, C. K. Chang, Y. C. Chuang, J. L. Zhang and R. R. Zhao, Selective doping for bond relaxation towards enhanced structural reversibility in Ni-rich layered cathodes, *Mater. Today Chem.*, 2022, **24**, 100926.

23 Y. Zhang, H. Li, J. Liu, J. Zhang, F. Cheng and J. Chen, $LiNi_{0.90}Co_{0.07}Mg_{0.03}O_2$ cathode materials with Mg-concentration gradient for rechargeable lithium-ion batteries, *J. Mater. Chem. A*, 2019, **7**(36), 20958–20964.

24 C. Roitzheim, L.-Y. Kuo, Y. J. Sohn, M. Finsterbusch, S. Möller, D. Sebold, H. Valencia, M. Meledina, J. Mayer, U. Breuer, P. Kaghazchi, O. Guillon and D. Fattakhova-Rohlfing, Boron in Ni-rich NCM811 cathode material: impact on atomic and microscale properties, *ACS Appl. Energy Mater.*, 2022, **5**(1), 524–538.

25 F. Xin, H. Zhou, X. Chen, M. Zuba, N. Chernova, G. Zhou and M. S. Whittingham, Li-Nb-O coating/substitution enhances the electrochemical performance of the $LiNi_{0.8}Mn_{0.1}Co_{0.1}O_2$ (NMC 811) cathode, *ACS Appl. Mater. Interfaces*, 2019, **11**(38), 34889–34894.

26 T. Weigel, F. Schipper, E. M. Erickson, F. A. Susai, B. Markovsky and D. Aurbach, Structural and electrochemical aspects of LiNi0.8Co0.1Mn0.1O2 cathode materials doped by various cations, *ACS Energy Lett.*, 2019, **4**(2), 508–516.

27 H. Lv, C. Li, Z. Zhao, B. Wu and D. Mu, A review: Modification strategies of nickel-rich layer structure cathode (Ni $\geq$ 0.8) materials for lithium ion power batteries, *J. Energy Chem.*, 2021, **60**, 435–450.

28 J. W. Fergus, Recent developments in cathode materials for lithium ion batteries, *J. Power Sources*, 2010, **195**(4), 939–954.

29 Y. Gao, J. Park and X. Liang, Comprehensive study of Al- and Zr-modified $LiNi_{0.8}Mn_{0.1}Co_{0.1}O_2$ through synergy of coating and doping, *ACS Appl. Energy Mater.*, 2020, **3**(9), 8978–8987.

30 J. Yan, H. Huang, J. Tong, W. Li, X. Liu, H. Zhang, H. Huang and W. Zhou, Recent progress on the modification of high nickel content NCM: coating, doping, and single crystallization, *Interdiscipl. Mater.*, 2022, **1**(3), 330–353.

31 S.-B. Kim, H. Kim, D.-H. Park, J.-H. Kim, J.-H. Shin, J.-S. Jang, S.-H. Moon, J.-H. Choi and K.-W. Park, Li-ion diffusivity and electrochemical performance of Ni-rich cathode material doped with fluoride ions, *J. Power Sources*, 2021, **506**, 230219.

32 B. Chu, Y.-J. Guo, J.-L. Shi, Y.-X. Yin, T. Huang, H. Su, A. Yu, Y.-G. Guo and Y. Li, Cobalt in high-energy-density layered cathode materials for lithium ion batteries, *J. Power Sources*, 2022, **544**, 231873.

33 W. Li, S. Lee and A. Manthiram, High-nickel NMA: a cobalt-free alternative to NMC and NCA cathodes for lithium-ion batteries, *Adv. Mater.*, 2020, **32**(33), 2002718.

34 H. Li, M. Cormier, N. Zhang, J. Inglis, J. Li and J. R. Dahn, Is cobalt needed in Ni-rich positive electrode materials for lithium ion batteries?, *J. Electrochem. Soc.*, 2019, **166**(4), A429.

35 S. Lee, W. Li, A. Dolocan, H. Celio, H. Park, J. H. Warner and A. Manthiram, In-depth analysis of the degradation mechanisms of high-nickel, low/No-cobalt layered oxide cathodes for lithium-ion batteries, *Adv. Energy Mater.*, 2021, **11**(31), 2100858.

36 H. Konishi, M. Yoshikawa and T. Hirano, The effect of thermal stability for high-Ni-content layer-structured cathode materials, $LiNi_{0.8}Mn_{0.1-x}Co_{0.1}Mo_xO_2$ ($x = 0$, 0.02, 0.04), *J. Power Sources*, 2013, **244**, 23–28.

37 H. Zhu, H. Yu, H. Jiang, Y. Hu, H. Jiang and C. Li, High-efficiency Mo doping stabilized $LiNi_{0.9}Co_{0.1}O_2$ cathode materials for rapid charging and long-life li-ion batteries, *Chem. Eng. Sci.*, 2020, **217**, 115518.

38 H.-H. Ryu, N.-Y. Park, D. R. Yoon, U.-H. Kim, C. S. Yoon and Y.-K. Sun, New class of ni-rich cathode materials $Li[Ni_xCo_yB_{1-x-y}]O_2$ for next lithium batteries, *Adv. Energy Mater.*, 2020, **10**(25), 2000495.

39 Z. Feng, R. Rajagopalan, S. Zhang, D. Sun, Y. Tang, Y. Ren and H. Wang, A three in one strategy to achieve zirconium doping, boron doping, and interfacial coating for stable $LiNi_{0.8}Co_{0.1}Mn_{0.1}O_2$ cathode, *Adv. Sci.*, 2021, **8**(2), 2001809.

40 Q. Liu, X. Su, D. Lei, Y. Qin, J. Wen, F. Guo, Y. A. Wu, Y. Rong, R. Kou, X. Xiao, F. Aguesse, J. Bareño, Y. Ren, W. Lu and Y. Li, Approaching the capacity limit of lithium cobalt oxide in lithium ion batteries *via* lanthanum and aluminium doping, *Nat. Energy*, 2018, **3**(11), 936–943.

41 X. Tan, W. Peng, M. Wang, G. Luo, Z. Wang, G. Yan, H. Guo, Q. Li and J. Wang, Al, Zr dual-doped cobalt-free nickel-rich cathode materials for lithium-ion batteries, *Prog. Nat. Sci.: Mater. Int.*, 2023, 1–8.

42 Y. Ming, W. Xiang, L. Qiu, W.-B. Hua, R. Li, Z.-G. Wu, C.-L. Xu, Y.-C. Li, D. Wang, Y.-X. Chen, B.-H. Zhong, F.-R. He and X.-D. Guo, Dual elements coupling effect induced modification from the surface into the bulk lattice

for ni-rich cathodes with suppressed capacity and voltage decay, *ACS Appl. Mater. Interfaces*, 2020, **12**(7), 8146–8156.

43 S. Jamil, A. Bin Yousaf, S. Hee Yoon, D. Suk Han, L. Yang, P. Kasak and X. Wang, Dual cationic modified high Ni-low co layered oxide cathode with a heteroepitaxial interface for high energy-density lithium-ion batteries, *Chem. Eng. J.*, 2021, **416**, 129118.

44 S. F. Amalraj, R. Raman, A. Chakraborty, N. Leifer, R. Nanda, S. Kunnikuruvan, T. Kravchuk, J. Grinblat, V. Ezersky, R. Sun, F. L. Deepak, C. Erk, X. Wu, S. Maiti, H. Sclar, G. Goobes, D. T. Major, M. Talianker, B. Markovsky and D. Aurbach, Boron doped Ni-rich $LiNi_{0.85}Co_{0.10}Mn_{0.05}O_2$ cathode materials studied by structural analysis, solid state NMR, computational modeling, and electrochemical performance, *Energy Storage Mater.*, 2021, **42**, 594–607.

45 F. A. Susai, D. Kovacheva, T. Kravchuk, Y. Kauffmann, S. Maiti, A. Chakraborty, S. Kunnikuruvan, M. Talianker, H. Sclar, Y. Fleger, B. Markovsky and D. Aurbach, Studies of nickel-rich $LiNi_{0.85}Co_{0.10}Mn_{0.05}O_2$ cathode materials doped with molybdenum ions for lithium-ion batteries, *Materials*, 2021, **14**(8), 2070.

46 F. A. Susai, D. Kovacheva, A. Chakraborty, T. Kravchuk, R. Ravikumar, M. Talianker, J. Grinblat, L. Burstein, Y. Kauffmann, D. T. Major, B. Markovsky and D. Aurbach, Improving performance of $LiNi_{0.8}Co_{0.1}Mn_{0.1}O_2$ cathode materials for lithium-ion batteries by doping with molybdenum-ions: theoretical and experimental studies, *ACS Appl. Energy Mater.*, 2019, **2**(6), 4521–4534.

47 S. S. Farvid, N. Dave, T. Wang and P. V. Radovanovic, Dopant-induced manipulation of the growth and structural metastability of colloidal indium oxide nanocrystals, *J. Phys. Chem. C*, 2009, **113**(36), 15928–15933.

48 K. Thieme, I. Avramov and C. Rüssel, The mechanism of deceleration of nucleation and crystal growth by the small addition of transition metals to lithium disilicate glasses, *Sci. Rep.*, 2016, **6**(1), 25451.

49 X. Luo, X. Wang, L. Liao, X. Wang, S. Gamboa and P. J. Sebastian, Effects of synthesis conditions on the structural and electrochemical properties of layered Li[Ni1/3Co1/3Mn1/3]O2 cathode material *via* the hydroxide co-precipitation method LIB SCITECH, *J. Power Sources*, 2006, **161**(1), 601–605.

50 J. N. Reimers, E. Rossen, C. D. Jones and J. R. Dahn, Structure and electrochemistry of $Li_xFe_yNi_{1-y}O_2$, *Solid State Ionics*, 1993, **61**(4), 335–344.

51 Y. Levartovsky, A. Chakraborty, S. Kunnikuruvan, S. Maiti, J. Grinblat, M. Talianker, D. T. Major and D. Aurbach, Enhancement of structural, electrochemical, and thermal properties of high-energy density Ni-rich $LiNi_{0.85}Co_{0.1}Mn_{0.05}O_2$ cathode materials for li-ion batteries by niobium doping, *ACS Appl. Mater. Interfaces*, 2021, **13**(29), 34145–34156.

52 O. Breuer, A. Chakraborty, J. Liu, T. Kravchuk, L. Burstein, J. Grinblat, Y. Kauffman, A. Gladkih, P. Nayak, M. Tsubery, A. I. Frenkel, M. Talianker, D. T. Major, B. Markovsky and D. Aurbach, Understanding the role of minor molybdenum doping in $LiNi_{0.5}Co_{0.2}Mn_{0.3}O_2$ electrodes: from structural and surface analyses and theoretical modeling to practical electrochemical cells, *ACS Appl. Mater. Interfaces*, 2018, **10**(35), 29608–29621.

53 H. Li, P. Zhou, F. Liu, H. Li, F. Cheng and J. Chen, Stabilizing nickel-rich layered oxide cathodes by magnesium doping for rechargeable lithium-ion batteries, *Chem. Sci.*, 2019, **10**(5), 1374–1379.

54 H. Chen, J. A. Dawson and J. H. Harding, Effects of cationic substitution on structural defects in layered cathode materials $LiNiO_2$, *J. Mater. Chem. A*, 2014, **2**(21), 7988–7996.

55 H. H. Sun, U.-H. Kim, J.-H. Park, S.-W. Park, D.-H. Seo, A. Heller, C. B. Mullins, C. S. Yoon and Y.-K. Sun, Transition metal-doped Ni-rich layered cathode materials for durable Li-ion batteries, *Nat. Commun.*, 2021, **12**(1), 6552.

56 J. Zheng, G. Teng, C. Xin, Z. Zhuo, J. Liu, Q. Li, Z. Hu, M. Xu, S. Yan, W. Yang and F. Pan, Role of Superexchange interaction on tuning of Ni/Li disordering in layered $Li(Ni_xMn_yCo_z)O_2$, *J. Phys. Chem. Lett.*, 2017, **8**(22), 5537–5542.

57 C. Delmas, M. Ménétrier, L. Croguennec, I. Saadoune, A. Rougier, C. Pouillerie, G. Prado, M. Grüne and L. Fournès, An overview of the $Li(Ni,M)O_2$ systems: syntheses, structures and properties, *Electrochim. Acta*, 1999, **45**(1), 243–253.

58 J. B. Goodenough and Y. Kim, Challenges for rechargeable Li batteries, *Chem. Mater.*, 2010, **22**(3), 587–603.

59 B. J. Hwang, Y. W. Tsai, D. Carlier and G. Ceder, A combined computational/experimental study on $LiNi_1/3Co_1/3Mn_1/3O_2$, *Chem. Mater.*, 2003, **15**(19), 3676–3682.

60 J. G. Speight, *Lange's Handbook of Chemistry*, McGraw-Hill Education, New York, 17th edn, 2017.

61 Y. Huang, Y.-C. Lin, D. M. Jenkins, N. A. Chernova, Y. Chung, B. Radhakrishnan, I.-H. Chu, J. Fang, Q. Wang, F. Omenya, S. P. Ong and M. S. Whittingham, Thermal stability and reactivity of cathode materials for li-ion batteries, *ACS Appl. Mater. Interfaces*, 2016, **8**(11), 7013–7021.

62 T. Sattar, S.-J. Sim, S.-G. Doo, B.-S. Jin and H.-S. Kim, A synergetic modification approach toward high capacity Ni-rich cathode materials for next generation lithium-ion batteries, *Solid State Ionics*, 2022, **387**, 116053.

63 H. W. Park, J. U. Hwang, J. S. Im and J. D. Lee, Electrochemical properties of LiNi0.9Co0.1O2 cathode material prepared by co-precipitation using an eco-friendly chelating agent, *J. Solid State Electrochem.*, 2022, **26**(8), 1567–1576.

64 F. Schipper, M. Dixit, D. Kovacheva, M. Talianker, O. Haik, J. Grinblat, E. M. Erickson, C. Ghanty, D. T. Major, B. Markovsky and D. Aurbach, Stabilizing nickel-rich layered cathode materials by a high-charge cation doping strategy: zirconium-doped $LiNi_{0.6}Co_{0.2}Mn_{0.2}O_2$, *J. Mater. Chem. A*, 2016, **4**(41), 16073–16084.

65 B. Hu, S. Jian, G. Yin, W. Feng, Y. Cao, J. Bai, Y. Lai, H. Tan and Y. Dong, Hetero-element-doped molybdenum oxide materials for energy storage systems, *Nanomaterials*, 2021, 1–16.

66 L. Dan, P. Hongrui and L. Guicun, Li_2MoO_4 coated $LiNi_{0.5}Co_{0.2}Mn_{0.3}O_2$ microspheres with enhanced lithium storage performances, in *Proceedings of the 6th*

International Conference on Mechatronics, Materials, Biotechnology and Environment (ICMMBE 2016), 2016/09, Atlantis Press, 2016, pp. 590–596.

67 H. W. Kwak and Y. J. Park, Li_2MoO_4 coated Ni-rich cathode for all-solid-state batteries, *Thin Solid Films*, 2018, **660**, 625–630.

68 J. U. Choi, N. Voronina, Y.-K. Sun and S.-T. Myung, Recent progress and perspective of advanced high-energy Co-less Ni-rich cathodes for li-ion batteries: yesterday, today, and tomorrow, *Adv. Energy Mater.*, 2020, **10**(42), 2002027.

69 T. Sattar, S.-H. Lee, B.-S. Jin and H.-S. Kim, Influence of Mo addition on the structural and electrochemical performance of Ni-rich cathode material for lithium-ion batteries, *Sci. Rep.*, 2020, **10**(1), 8562.

70 C.-J. Lin and W.-C. J. Wei, Grain boundary pinning of polycrystalline Al_2O_3 by Mo inclusions, *Mater. Chem. Phys.*, 2008, **111**(1), 82–86.

